Supplementary Information

to accompany the article

Field-induced quasi-bound state within the two-magnon continuum of a square-lattice Heisenberg antiferromagnet

F. Elson, M. Nayak, A. A. Eberharter, M. Skoulatos, S. Ward, N. B. Christensen, D. Voneshen, C. Fiolka, K. W. Krämer, Ch. Rüegg, H. M. Rønnow, B. Normand, M. Mourigal, F. Mila, A. M. Läuchli and M. Månsson

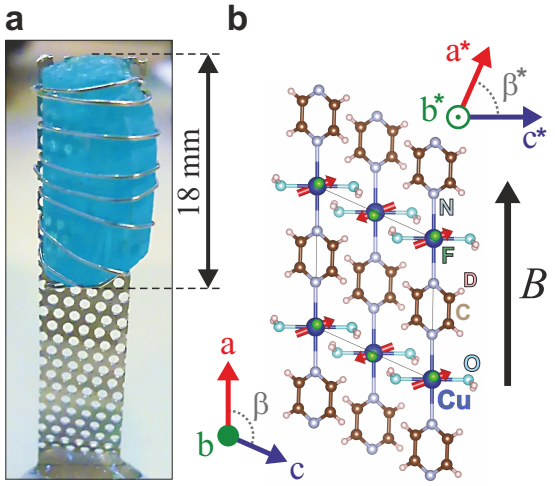

Figure S1: **Single-crystal mount and crystal structure of $CuF_2(D_2O)_2(pyz)$. a** Photograph of the sample used in our scattering experiments. **b** Representation of the stacking of square-lattice planes in the crystal structure, viewed along the b axis and with the zero-field magnetic structure represented by the red arrows.

S1. CRYSTAL AND EXPERIMENTAL GEOMETRY

Large single crystals of $CuF_2(D_2O)_2(pyz)$ were grown as detailed in the Methods section. Powder X-ray diffraction on crushed crystals was used to determine their phase purity and to perform an initial Rietveld structural refinement, as described in Ref.[S1] A further refinement of the crystal structure was performed on elastic scattering cuts from our time-of-flight data; this verified the monoclinic $P2_1/c$ space group with lattice parameters $a = 7.56$ Å, $b = 7.44$ Å, $c = 6.82$ Å, $\alpha = \gamma = 90.00°$ and $\beta = 113.66°$.

Figure S1a shows a photograph of our single-crystal sample aligned on an aluminium sample holder with the b^*c^* plane [$(0\ K\ L)$ plane] horizontal and the magnetic field along the a axis ([100] axis). Figure S1b shows a real-space representation of the crystal viewed along the b axis ([010] axis). The square lattice of interacting Cu^{2+} ions is the bc plane of $CuF_2(D_2O)_2(pyz)$, with the weak interplane interactions along the a axis. The zero-field magnetic structure of the material, which includes a tilting of the spins out of the bc plane and towards the a axis, is shown by the red arrows.

Elastic cuts through our LET data in the $(0, K, L)$, $(H, K, 1)$ and $(H, 1, L)$ planes are shown in Fig. S2. The match between the nuclear Bragg peaks and the reciprocal-lattice grid reflects the accuracy of our crystal alignment and refined structural parameters. This demonstration is important to determine the monoclinic angle β accurately; this angle enters the neutron scattering cross-section in the dipole projection factor and hence impacts the magnetic intensity resulting from integrating the signal in the out-of-plane direction.

S2. INELASTIC NEUTRON SCATTERING

In our LET experiment we chose the three incident energies $E_i = 2.67$, 5.50 and 13.85 meV in order to explore the full bandwidth of the magnetic excitations in $CuF_2(D_2O)_2(pyz)$. In the main text we focused on our $E_i = 5.50$ meV data, which provided the best compromise between energy resolution and energy range. For completeness, here we present further analysis of our $E_i = 2.67$ and 13.85 meV measurements, highlighting the field-dependence of selected momentum-energy slices in Figs. S3 and S4.

It is evident in Fig. S3 that the momentum-energy coverage at $E_i = 2.67$ meV is significantly smaller than that at $E_i = 5.50$ meV, making this incident energy too low to capture the Larmor-shadow mode (LSM). However, it is sufficient to capture the entire one-magnon bandwidth, and indeed with a FWHM energy resolution significantly sharper than for $E_i = 5.5$ meV. Nevertheless, we find that the one-magnon excitations remain resolution-limited.

Turning to $E_i = 13.85$ meV, the considerably larger momentum-energy coverage allows us to follow the evolution of all spectral features, including the LSM, through multiple Brillouin zones. Figure S4 confirms that this mode is a ubiquitous feature of the dynamical response. This dataset also illustrates the absence of significant phonon contributions below $E \approx 5$ meV, whereas the mode around $E = 6$ meV, whose intensity increases with momentum transfer for the $(0, K, K)$ and $(0, 0, K)$ slices, is an optical phonon.

Measurements with variable E_i also confirm our statement that the band of intensity around 1.2 meV in Fig. 2 of the main text is a consequence of scattering from the LET magnet. It is simply absent at lower E_i, where the

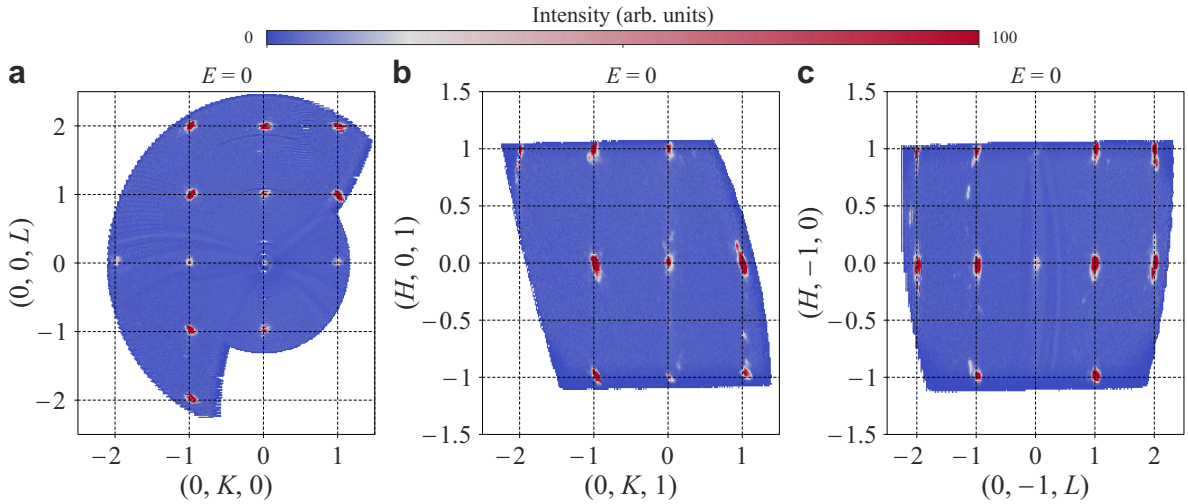

Figure S2: **Quality of single-crystal alignment on LET.** Elastic neutron scattering intensity from our $CuF_2(D_2O)_2(pyz)$ crystal for incident energy $E_i = 13.85$ meV, sliced in the **a-c** $(0, K, L)$, $(H, K, 1)$ and $(H, -1, L)$ planes, respectively, covering several repeated Brillouin zones.

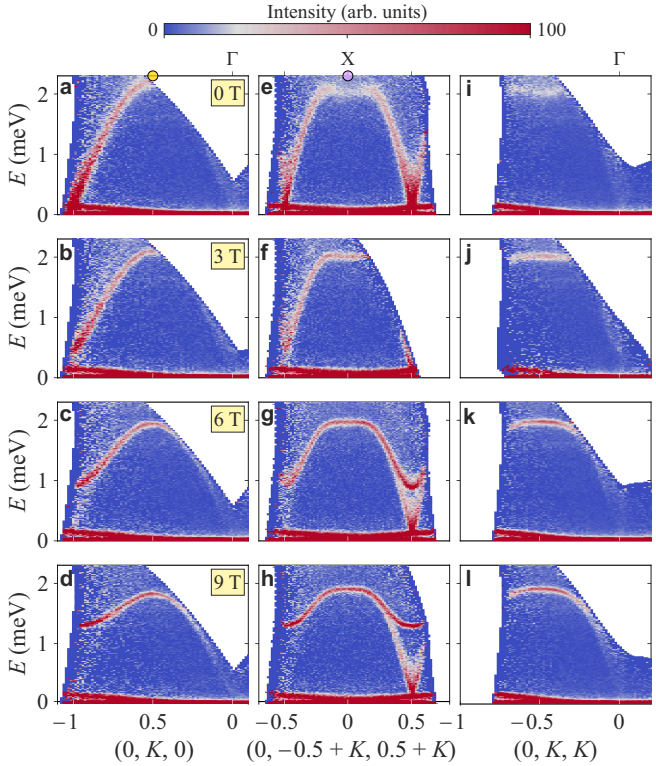

Figure S3: **Field-dependence of magnetic excitations measured on LET with $E_i = 2.67$ meV.** Momentum-energy slices through the data are shown with the momentum transfer K (measured in r.l.u.) varying along **a-d** $(0, K, 0)$, **e-h** $(0, -0.5 + K, 0.5 + K)$, and **i-l** $(0, K, K)$.

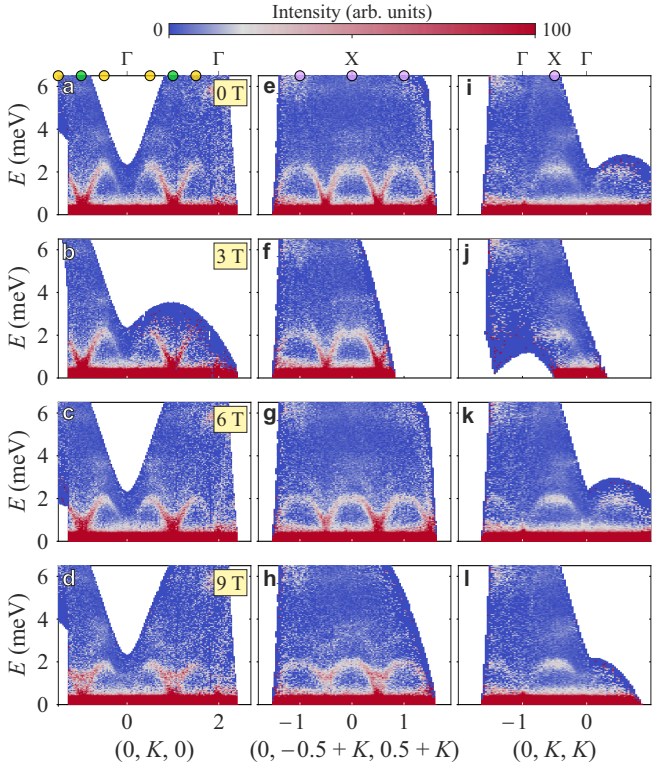

Figure S4: **Field-dependence of magnetic excitations measured on LET with $E_i = 13.85$ meV.** Momentum-energy slices shown along the same directions as in Fig. S3.

low-energy signal visible in Fig. S3 that seemingly disperses from the elastic line is a different type of spurion that arises from multiple scattering within the magnet.

At higher E_i, the reflected neutrons arrive more quickly at the detector and the spurion appears at a low energy indistinguishable from the elastic line. We reiterate that the invariance of this feature with changing applied field and its absence in our TASP data also mark it unam-

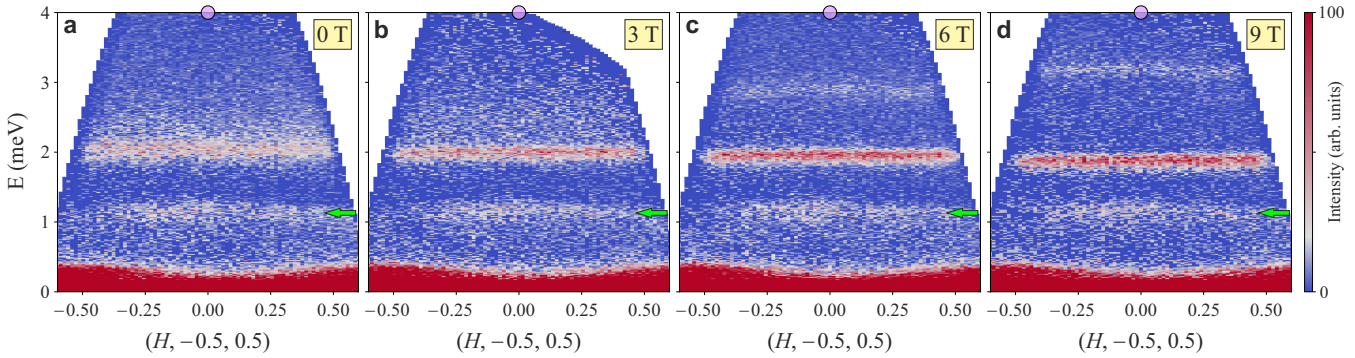

Figure S5: **Out-of-plane dispersion of magnetic excitations measured on LET with $E_i = 5.50$ meV.** Field-dependence of flat excitations along the $(H, 0, 0)$ direction, centred around the $(0, -0.5, 0.5) \equiv (\pi, 0)$ point of the square-lattice Brillouin zone of $CuF_2(D_2O)_2$(pyz). Green arrows at $E = 1.2$ meV indicate again the field-independent spurious scattering signal that is present in our $E_i = 5.50$ meV data (Fig. 2 of the main text) but absent at $E_i = 2.67$ meV (Fig. S3) and 13.8 meV (Fig. S4).

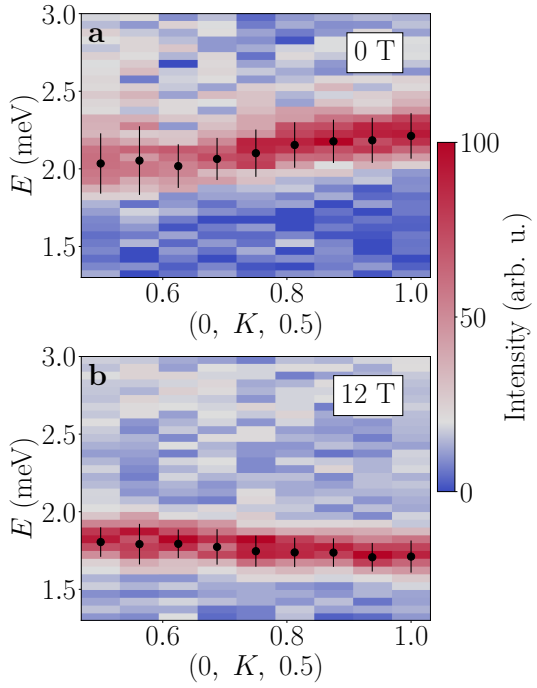

Figure S6: **Field-dependence of zone-boundary excitations measured on TASP. a** One-magnon dispersion along the zone boundary from $(0, 0.5, 0.5) \equiv (\pi, 0)$ to $(0, 1, 0.5) \equiv (\pi/2, \pi/2)$ at 0 T. **b** Zone-boundary one-magnon dispersion at 12 T.

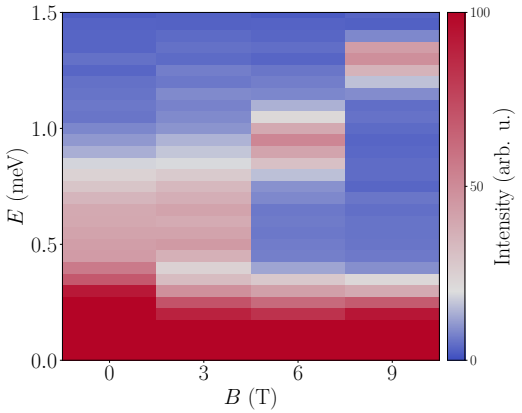

Figure S7: **Field-dependence of the Larmor mode.** Energy of the gapped one-magnon branch at the M point, shown as a function of the magnetic field applied in our LET experiment. This gap measures the Larmor energy, $E_L = g\mu_B\mu_0 B$.

biguously as a spurion.

To investigate the out-of plane dispersion (i.e. along the a^* direction) we prepared additional slices through the $E_i = 5.50$ meV dataset to focus specifically on $(H, -0.5, 0.5)$, which is centred on the zone-boundary $(\pi, 0)$ point in square-lattice units. As Fig. S5 makes clear, both the zone-boundary one-magnon mode and the LSM have minimal dispersion at all magnetic fields measured. This is particularly clear at 6 T and 9 T, where the energies remain completely constant despite the momentum transfer spanning an entire Brillouin zone. These results justify our assumption that the magnetic interactions in $CuF_2(D_2O)_2$(pyz) are strictly two-dimensional.

Figure S6 complements Fig. 4 of the main text, which showed the detailed dependence on magnetic field of the spectra measured on TASP at $(0, 0.5, 0.5) \equiv (\pi, 0)$ and $(0, 1, 0.5) \equiv (\pi/2, \pi/2)$, by presenting momentum scans performed at 0 T and 12 T that connect these points. It is clear that a magnetic field of 12 T causes a significant decrease in the energy of the zone-boundary one-magnon branch, and also a significant sharpening of this branch. The reduction in linewidth is present not only at $(\pi, 0)$, where increasing magnetic field eliminates the scattering anomaly, but in a less pronounced form for all momenta along the zone boundary. The LSM is not visible in these TASP datasets because it has not formed at 0 T and lies outside the available energy range at 12 T.

Figure S7 complements Fig. 2 of the main text, by

presenting the energy of the gapped mode at the M point $(0,-1,0)$ as a function of the magnetic field. Because of the unit-cell doubling in the ordered phase, this gap constitutes a measurement of the Larmor mode, and a fit to the linear field-dependence allows us to extract a g-factor for this field direction of $g_a \approx 2.4$.

S3. CYLINDER MATRIX-PRODUCT-STATES CALCULATIONS

Matrix-product states (MPS) provide an Ansatz that allows a highly efficient representation of the quantum many-body states of a 1D Hamiltonian. The MPS is formulated using rank-three tensors at each lattice site and the accuracy of the Ansatz is determined by the bond dimension, χ. MPS methods can be extended to 2D systems by wrapping the lattice in a cylindrical geometry, keeping periodic boundary conditions in the wrapping direction and open boundary conditions at the edges of the cylinder. Calculation of the dynamical spin structure factor (DSSF) proceeds in two steps, (i) determining the ground state of the Hamiltonian and (ii) time-evolving the system by applying the appropriate spin operators to this state. The ground state is obtained using the density-matrix renormalization group (DMRG), which is an iterative variational algorithm. Time-evolution of the state resulting from the action of a spin operator on the ground state is effected by the time-dependent variational principle (TDVP). The two-site variant of the TDVP algorithm trotterizes the projectors to the tangent space of the MPS for every adjacent pair of sites, and applying these projectors results in an effective two-site Hamiltonian. The exponential of the effective Hamiltonian ($e^{-i\frac{1}{2}H_{\rm eff}\delta t}$) acts on the MPS to give the local time-evolution, which is iterated over all sites from the left to the right end of the MPS and then back. The result is the new state time-evolved by one time step, δt. The final time to which the state is evolved is denoted by t_f and the number of steps by N (i.e. $t_f = N\delta t$).

A. Ground-state order

We perform our calculations in the laboratory frame (x_0, y_0, z_0) defined in the main text, where the external magnetic field is aligned in the z_0 direction. This allows us to distinguish the component $\mathcal{S}^{z_0 z_0}$ of the DSSF involving spin fluctuations parallel to the field, denoted $\parallel B$, from the components perpendicular to the field ($\perp B$). In order to reproduce both the INS results and the known ordered moment of the SLHAF, $m_0 = 0.61\mu_0$, we include a small symmetry-breaking staggered field in the x_0 direction, and hence model the spin Hamiltonian

$$H = J\sum_{\langle i,j\rangle}\mathbf{S}_i\cdot\mathbf{S}_j + h_z\sum_{i,j}S^{z_0}_{i,j} + h_x\sum_{i,j},(-1)^{i+j}S^{x_0}_{i,j}, \quad \text{(S1)}$$

where J is the nearest-neighbour spin-spin interaction, h_z the external magnetic field and h_x the staggered field. To access the complete spectra for the two different high-symmetry lines in the Brillouin zone shown in Fig. 2 of the main text, we wrapped the square lattice onto the cylinder in two different ways, namely horizontal and diagonal (i.e. a 45° tilt of the lattice). MPS calculations were performed at the magnetic fields corresponding to the LET measurements, B = 0, 3, 6 and 9 T, using a cylinder of length $L = 100$ and circumferences of $w = 4$ and 6, with bond dimension $\chi = 400$.

The staggered field required to obtain the staggered and uniform magnetizations computed by ED and by QMC simulations[S2] within a tolerance of 10^{-2} was determined to be $h_x = 0.01J$. As expected, the presence of this tiny field made no difference to the excitation energies (within the effective energy resolution), but led to a discernible reduction in the spectral intensity of the one-magnon branch in the $\mathcal{S}^{x_0x_0}$ channel, with a concomitant increase in $\mathcal{S}^{y_0y_0}$; after multiplication of each with their respective polarization factors we reproduce the results measured by INS.

B. Dynamical spin structure factor

Because the magnetic order of the ground state is uniform in $\langle S^{z_0}\rangle$ and staggered in $\langle S^{x_0}\rangle$, the magnetic unit cell contains $n_c = 2$ sites. We compute the time-dependent spin-spin correlations starting from each of these sites and take the Fourier transform

$$\mathcal{S}^{\alpha\beta}(\mathbf{k},\omega) = \frac{1}{n_c}\sum_{a,b} e^{-i\mathbf{k}\cdot(\mathbf{r}_a-\mathbf{r}_b)}S^{\alpha\beta}_{a,b}(\mathbf{k},\omega), \quad \text{(S2)}$$

with $\mathbf{r}_a$ and $\mathbf{r}_b$ the relative positions of sites a and b within the unit cell and

$$\begin{aligned} S^{\alpha\beta}_{a,b}(\mathbf{k},\omega) &= \frac{1}{N_c}\sum_{\mathbf{R}}\int_{-\infty}^{\infty} e^{i(\omega t-\mathbf{k}\cdot\mathbf{R})}C^{\alpha,\beta}_{\mathbf{R},\mathbf{0}}(t)dt, \quad \text{(S3)}\\ C^{\alpha,\beta}_{\mathbf{R},\mathbf{0}}(t) &= \langle S^{\alpha}_{a,\mathbf{R}}(t)S^{\beta}_{b,\mathbf{0}}(0)\rangle - \langle S^{\alpha}_{a,\mathbf{R}}(0)\rangle\langle S^{\beta}_{b,\mathbf{0}}(0)\rangle, \end{aligned}$$

where N_c is the number of unit cells, $\mathbf{R}$ the spatial position of each cell and $\alpha = \beta \in \{x_0, y_0, z_0\}$ are the spin components. The spread of the time-dependent spin-spin correlations limits the maximum time up to which a state can be evolved. The long cylinders we choose set an upper limit of $t_f = 32/J$ before a spin operation at the centre of the cylinder can reach the open boundaries. Setting this cut-off prevents Friedel oscillations, which would introduce uncontrolled numerical artifacts in the spectra. To avoid the Gibbs oscillations that arise due to the finite evolution time, it is standard to multiply $C^{\alpha,\beta}_{\mathbf{R},\mathbf{0}}(t)$ by a Gaussian filter in time when performing the Fourier transform. This filter function is expressed as

$$f(t) = \frac{1}{\sqrt{2\pi\sigma_t^2}}e^{-t^2/2\sigma_t^2},$$

where we set $\sigma_t = \frac{1}{2}t_f$.

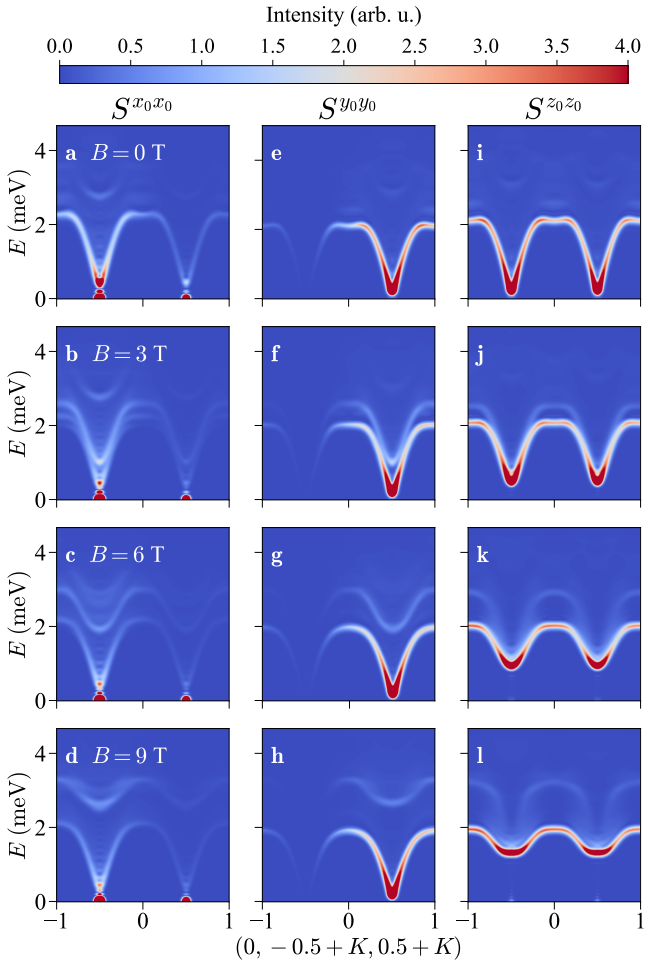

Figure S8: **DSSF along MXM calculated by MPS for the three separate spin channels.** The DSSF components $\mathcal{S}^{x_0x_0}$ (a-d), $\mathcal{S}^{y_0y_0}$ (e-h) and $\mathcal{S}^{z_0z_0}$ (i-l) with polarization factor are shown for the four magnetic fields of the LET experiment and for the $(0, -0.5 + K, 0.5 + K)$ direction.

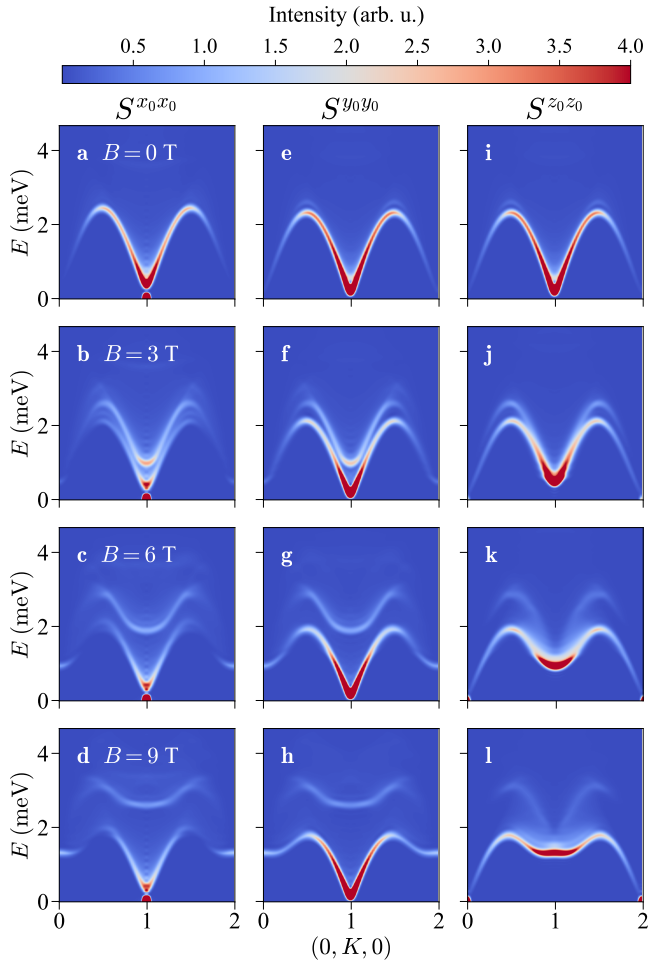

Figure S9: **DSSF along ΓMΓ calculated by MPS for the three separate spin channels.** The DSSF components $\mathcal{S}^{x_0x_0}$ (a-d), $\mathcal{S}^{y_0y_0}$ (e-h) and $\mathcal{S}^{z_0z_0}$ (i-l) are shown for the four magnetic fields of the LET experiment and for the $(0, K, 0)$ direction (Figs. 2(a-h) of the main text). The polarization factor is not included because it is uniformly unity for $\mathcal{S}^{x_0x_0}$ and $\mathcal{S}^{z_0z_0}$, and uniformly zero for $\mathcal{S}^{y_0y_0}$.

C. Spin channels and polarization factor

The external magnetic field fixes the direction z_0 (corresponding to the crystalline a axis) and the staggered field is applied in the x_0 direction, meaning that the ordered moments have no component along y_0, which then corresponds to the c^* axis. The polarization factor in the INS cross-section modulates the components of the DSSF according to

$$P_\alpha(\mathbf{Q}) = \left(1 - \frac{Q_\alpha^2}{\mathbf{Q}^2}\right), \tag{S4}$$

where $\mathbf{Q} = H\mathbf{a}^* + K\mathbf{b}^* + L\mathbf{c}^*$ and the components are expressed in the laboratory frame, meaning that $\alpha \in \{x_0, y_0, z_0\}$, corresponding to the $(c^*, -b^*, a)$ directions in the crystal. The total INS cross section then satisfies

$$I(\mathbf{Q}, \omega) \propto \sum_\alpha P_\alpha(\mathbf{Q}) S^{\alpha\alpha}(\mathbf{Q}, \omega), \tag{S5}$$

where $S^{\alpha\alpha}(\mathbf{Q}, \omega)$ is defined in Eq. (S2).

The separate spin channels $\mathcal{S}^{x_0x_0}$, $\mathcal{S}^{y_0y_0}$ and $\mathcal{S}^{z_0z_0}$ obtained from MPS are shown in Fig. S8 for the $(0, -0.5 + K, 0.5 + K)$ direction, which corresponds to the experimental measurements shown in Figs. 2i-l of the main text, while the sum of these three components is shown in Figs. 2m-p. We observe that each channel contains only one magnon branch and one LSM, but that these are not of the same character, with the exact E_L-shifted copy of a given branch in $\mathcal{S}^{x_0x_0}$ and $\mathcal{S}^{y_0y_0}$ (which are the same up to polarization factors) appearing in $\mathcal{S}^{z_0z_0}$ and conversely. In Fig. S9 we separate the spin channels for the DSSF in the $(0, K, 0)$ direction, which corresponds to the measurements shown in Figs. 2a-d of the main text, with the sum of the three components in Figs. 2e-h. Here we do not include the polarization factor, which is independent of K; this factor multiplies the $\mathcal{S}^{y_0y_0}$ channel by

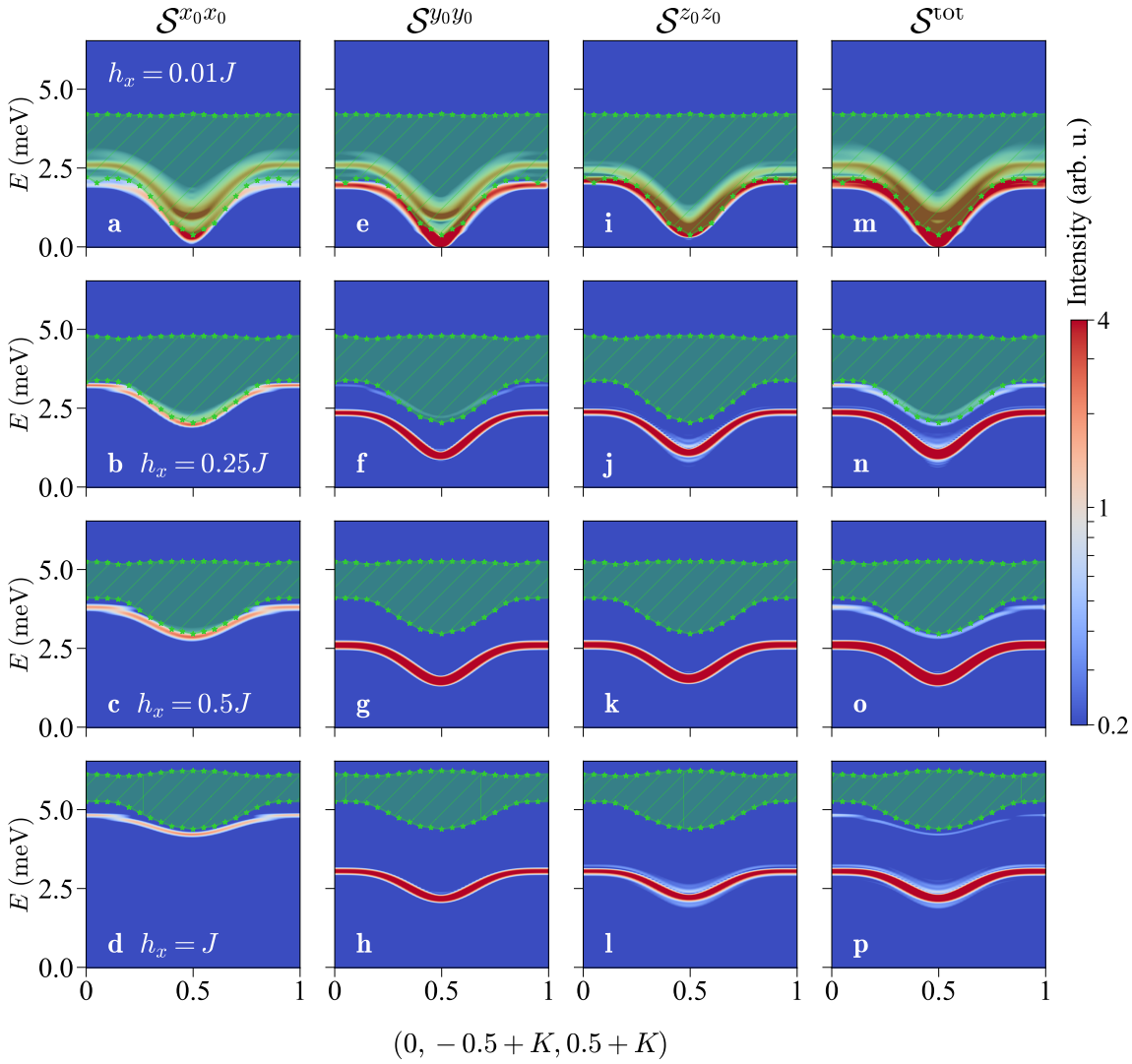

Figure S10: **Characteristics of the LSM at different staggered magnetic fields.** DSSF components $S^{x_0x_0}$ (a-d), $S^{y_0y_0}$ (e-h), $S^{z_0z_0}$ (i-l) and their sum combined with the INS polarization factor, denoted S_{tot} (m-p), shown for the XMX direction (specifically, $(0, -0.5+K, 0.5+K)$) at different h_x values and a fixed longitudinal field of $B = 3$ T. We use a logarithmic colour scale to highlight the LSM. The magnitude of staggered field is increased from top to bottom, taking the values $h_x = 0.01J$ (a,e,i,m), $0.25J$ (b,f,j,n), $0.5J$ (c,g,k,o) and J (d,h,l,p). The two-magnon continuum is represented by the green shading (based on the boundary points represented by the small stars). The bound state is visible most prominently in the $S^{x_0x_0}$ channel and lies outside the two-magnon continuum for the full range of k_x at $h_x = J$.

zero, such that it makes no contribution to the DSSF, but we show it for for completeness. Again we observe the same branches in $\mathcal{S}^{x_0x_0}$ and $\mathcal{S}^{y_0y_0}$ and the channel-switching nature of the processes forming the two LSMs.

We stress that, when comparing our MPS results with INS in Fig. 2 of the main text, the same scale factor is used at all four applied magnetic fields. We remark also that, in making this type of comparison, we have not modelled the instrumental resolution function in detail, but instead choose the width of the Gaussian filter in our MPS calculations (Sec. S3B) to achieve an approximate linewidth match; again only one value of σ_t is used throughout. These comparisons provide a complete validation of the SLHAF as the model and for the orientation of the canted magnetic structure with respect to the crystal axes, specifically that they rotate in the ac^* plane as the field is increased.

D. Nature of the Larmor-Shadow Mode

In the main text we showed that the primary hallmarks of the LSM observed by INS and MPS are its shift by the Larmor energy from the one-magnon branch and its very sharp (albeit intrinsic) linewidth. However, this mode lies within the boundaries of the conventional two-magnon continuum, and hence it is expected to be an anomalously narrow resonance, or quasi-bound state,

rather than being a true bound state. One way to investigate how the resonance we observe is related to a true bound state is to increase the staggered-field parameter (h_x) in our MPS calculations based on the Hamiltonian of Eq. (S1).

The first step of this analysis is to determine the boundaries of the two-magnon continuum. A robust calculation of the one-magnon dispersion on a dense grid of evenly spaced momenta in (k_x, k_y) would lead directly to the continuum boundaries for two noninteracting magnons. An unbiased calculation of the magnon dispersion can be effected by following the intensity maximum in the MPS DSSF. However, the finite circumference of the cylinder restricts this exercise to a limited number of k_y values, specifically $k_y = 0$, $\pi/2$, π and $3\pi/2$ for $w = 4$ and in addition $k_y = \pi/3$, $2\pi/3$, $4\pi/3$ and $5\pi/3$ with $w = 6$. To obtain an adequately dense grid in k_y, we interpolate between the available values over the range from 0 and 2π by describing the magnon dispersion as a sum of cosines,

$$\omega(k_x, k_y) = \sum_{n=0}^{5} a_n(k_x) \cos(n k_y),$$

fitted to the DSSF data. The upper and lower boundaries of the two-magnon continuum are then given by

$$\begin{aligned} \omega_{\rm u}(K_x, K_y) &= \max[\omega(k_{x_1}, k_{y_1}) + \omega(k_{x_2} + \pi, k_{y_2} + \pi)], \\ \omega_{\rm l}(K_x, K_y) &= \min[\omega(k_{x_1}, k_{y_1}) + \omega(k_{x_2} + \pi, k_{y_2} + \pi)], \end{aligned}$$

where $K_x = k_{x_1} + k_{x_2} \mod 2\pi$ and $K_y = k_{y_1} + k_{y_2} \mod 2\pi$. We estimate the uncertainties in this procedure from the fact that width-4 and width-6 cylinders share two wavevectors, and the differences in magnon energies at these two points lie within $0.025J$ for all values of k_x. These differences are finite-size effects, and taking the uncertainty in the magnon dispersion relation to be $0.025J$ sets the error bars on the upper and lower boundaries of the two-magnon continuum as $0.05J$.

Figure S10 shows the separate spectral functions in all three spin channels for four representative values of h_x. Considering first the one-magnon branches, the h_x value we used to model $CuF_2(D_2O)_2$(pyz) (Figs. S10a,e,i) has no effect other than to remove the U(1) rotational symmetry. Increasing h_x causes the progressive opening of a full gap, a flattening of the bandwidth and an increase in the band centre, which together cause a progressive raising and narrowing of the two-magnon continuum. By comparing its location to the boundaries of this continuum, one may trace the evolution of the LSM in the $\perp B$ spin channels from a rather sharp resonance within the continuum at small h_x to a well defined (resolution-limited) and separate mode lying completely below the continuum as h_x approaches J.

In that limit, h_x dominates both B and J to enforce a ground state with staggered spin orientation in the x_0 direction. One-magnon excitations can arise only due to the action of S^{y_0} or S^{z_0} in flipping the spins of this state, and hence appear only in the $S^{y_0 y_0}$ and $S^{z_0 z_0}$ channels. The bound state is a distinct and stable mode arising from two spin-flips that are adjacent, giving them an energy J lower than two independent spin-flips. Although this mode appears in both $S^{x_0 x_0}$ and $S^{y_0 y_0}$, the absence of an intense one-magnon branch in $S^{x_0 x_0}$ makes it straightforward to track the evolution of the bound state into a resonance with decreasing h_x in this channel.

S4. SPIN-WAVE THEORY

Spin-wave theory (SWT) provides a systematic framework in which to interpret the properties of ordered magnetic systems. Despite the technical complexities inherent to any expansion beyond the lowest orders, this framework nevertheless affords considerable insight into the microscopic spin-fluctuation processes underlying many of the physical properties displayed even by systems with strong quantum fluctuations. With a view to obtaining deeper insight into the origin of the LSM, we applied SWT including $1/S$ corrections to calculate the zero-temperature DSSF of the quasi-2D square-lattice Heisenberg antiferromagnet (SLHAF) following the approach of Ref.[S3] It is straightforward to adapt this calculation to the geometry of our $CuF_2(D_2O)_2$(pyz) experiments and hence to compare its output with our INS and cylinder MPS results.

A. General geometrical considerations

We consider the Hamiltonian

$$H = J \sum_{\langle ij \rangle} \mathbf{S}_i \cdot \mathbf{S}_j + J' \sum_{\langle ij \rangle_z} \mathbf{S}_i \cdot \mathbf{S}_j - g\mu_B B \sum_i S_i^{z_0}, \quad \text{(S6)}$$

with the magnetic field applied along the z_0 direction in the laboratory frame ($z_0 \equiv [100]$ matches the a axis in our sample alignment, with the b^*c^* plane horizontal). Here g is the gyromagnetic ratio of the Cu^{2+} magnetic moments in the field direction and in addition to the nearest-neighbour J in the crystallographic bc plane we consider an interplane interaction J' parametrized by $\alpha = J'/J$ ($0 \leq \alpha \leq 1$). Both interactions are antiferromagnetic and α in $CuF_2(D_2O)_2$(pyz) is demonstrably very small, but sufficient to stabilize long-range magnetic order at the Néel temperature, $T_{\rm N} = 2.6$ K.

To calculate the spin components in the Cartesian laboratory frame $(\hat{x}_0, \hat{y}_0, \hat{z}_0)$, we assume a canted antiferromagnetic order for any $B > 0$, as shown in Fig. S11. This order is associated with the propagation vector $\mathbf{Q}_m = (\pi, \pi, \pi)$ and with a field-dependent canting angle, θ, by which the spins tilt uniformly out of the spin-flop plane, which is that perpendicular to B. The wavevector $\mathbf{Q}_0 = (0, 0, 0)$ corresponding to the uniform magnetization can be viewed as a secondary propagation vector. The U(1) symmetry of this system corresponds to one

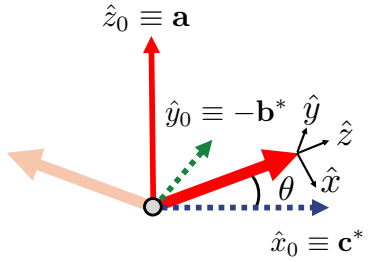

Figure S11: **Canted magnetic structure.** Depiction of the assumed magnetic order within the laboratory frame, $(\hat{x}_0, \hat{y}_0, \hat{z}_0)$, which defines the local frame, $(\hat{x}, \hat{y}, \hat{z})$.

remaining degree of freedom, the spin projection in the x_0y_0 (b^*c^*) plane, which we express as ϕ measured from the x_0 axis and assume to be independent of θ.

In $CuF_2(D_2O)_2$(pyz) at zero field the spins are aligned along $[0.7, 0, 1]$ in real space, meaning that there is no ordered component along $\hat{b} \equiv [0, 1, 0]$, which coincides with $\hat{b}^*$. Thus we assume that, just after the spin-flop ($B = 0^+$), the spins align perpendicular to the field direction ($\hat{a}$) and perpendicular to $\hat{b}^*$, i.e. that the spins point initially along $\hat{c}^* \equiv (0, 0, 1)$ and tilt gradually towards $\hat{a}$ with increasing field. To maintain a right-handed coordinate system, we set $\hat{x}_0$ along $c^* \equiv (0, 1, 0)$ ($\phi = 0$) and thus $\hat{y}_0$ along $-b^* \equiv (0, 0, \bar{1})$. Finally, based on the parameters we use to model $CuF_2(D_2O)_2$(pyz) ($J = 0.934$ meV, $\alpha = 0.01$, $B_{\mathrm{sat},a} = 28.6$ T, $g_a = 2.4$), we expect θ to range from 0 to $\theta_{\max} \approx \arcsin(0.4) = 23.6°$ at fixed $\phi = 0$.

The relationship between spin components in the local and laboratory frames is[S3]

$$\begin{aligned} S_i^{z_0} &= \sin\theta S_i^z - e^{i\mathbf{Q}_m\cdot\mathbf{r}_i}\cos\theta S_i^x, \\ S_i^{y_0} &= e^{i\mathbf{Q}_m\cdot\mathbf{r}_i}\cos\theta\sin\phi S_i^z + \cos\phi S_i^y + \sin\theta\sin\phi S_i^x, \\ S_i^{x_0} &= e^{i\mathbf{Q}_m\cdot\mathbf{r}_i}\cos\theta\cos\phi S_i^z + \sin\phi S_i^y + \sin\theta\cos\phi S_i^x, \end{aligned} \tag{S7}$$

which for $\phi = 0$ yields

$$\begin{aligned} S_i^{z_0} &= \sin\theta S_i^z - e^{i\mathbf{Q}_m\cdot\mathbf{r}_i}\cos\theta S_i^x, \\ S_i^{y_0} &= S_i^y, \\ S_i^{x_0} &= e^{i\mathbf{Q}_m\cdot\mathbf{r}_i}\cos\theta S_i^z + \sin\theta S_i^x. \end{aligned} \tag{S8}$$

The Fourier transform $S_{\mathbf{k}}^{\alpha} = (1/\sqrt{N})\sum_i e^{-i\mathbf{k}\cdot\mathbf{r}_i} S_i^{\alpha}$ then leads to

$$\begin{aligned} S_{\mathbf{k}}^{z_0} &= \sin\theta S_{\mathbf{k}}^z - \cos\theta S_{\mathbf{k}-\mathbf{Q}_m}^x, \\ S_{\mathbf{k}}^{y_0} &= S_{\mathbf{k}}^y, \\ S_{\mathbf{k}}^{x_0} &= \cos\theta S_{\mathbf{k}-\mathbf{Q}_m}^z + \sin\theta S_{\mathbf{k}}^x. \end{aligned} \tag{S9}$$

We define the component $\alpha\beta$ of the DSSF as

$$\mathcal{S}^{\alpha\beta}(\mathbf{k},\omega) = \int \frac{\mathrm{d}t}{2\pi} e^{i\omega t}\langle S_{\mathbf{k}}^{\alpha}(t) S_{-\mathbf{k}}^{\beta}(0)\rangle \tag{S10}$$

and obtain the diagonal components in the laboratory frame in the form

$$\begin{aligned} \mathcal{S}^{z_0z_0}(\mathbf{k},\omega) &= \sin^2\theta\,\mathcal{S}^{zz}(\mathbf{k},\omega) + \cos^2\theta\,\mathcal{S}^{xx}(\mathbf{k}-\mathbf{Q}_m,\omega), \\ \mathcal{S}^{y_0y_0}(\mathbf{k},\omega) &= \mathcal{S}^{yy}(\mathbf{k},\omega), \\ \mathcal{S}^{x_0x_0}(\mathbf{k},\omega) &= \cos^2\theta\,\mathcal{S}^{zz}(\mathbf{k}-\mathbf{Q}_m,\omega) + \sin^2\theta\,\mathcal{S}^{xx}(\mathbf{k},\omega), \end{aligned} \tag{S11}$$

where following previous studies[S3–S5] we have neglected components off-diagonal in the local frame.

For an explicit definition of terminology, we remark that spin fluctuations appearing in the xx and yy response functions are transverse to the ordered moments and typically are dominated by one-magnon excitations. In the laboratory frame, these terms appear at wavevector $\mathbf{k}$ in the $\perp B$ (in-plane) channel, while spin fluctuations in xx also appear at wavevector $\mathbf{k} - \mathbf{Q}_m$ in the $\parallel B$ (out-of-plane) channel. The situation is reversed for spin fluctuations appearing in zz, which are longitudinal with the ordered moment, are usually dominated by two-magnon excitations and appear at wavevector $\mathbf{k}$ ($\mathbf{k}-\mathbf{Q}_m$) in the $\parallel B$ ($\perp B$) channel. In the main text we defined the notation for these channels as $\mathcal{S}^{\alpha\alpha}_{\perp B}$ and $\mathcal{S}^{\alpha\alpha}_{\parallel B}$, where the superscript indicates components in the local frame and the subscripts refer to their projection in the laboratory frame.

After applying the magnetic form and projection factors, the scattered intensity at transferred momentum $\mathbf{Q}$ and energy $E = \hbar\omega$ is

$$\begin{aligned} \mathcal{I}(\mathbf{Q},\omega) &= r_0^2|f(Q)|^2\big\{g_a^2\mathcal{S}^{z_0z_0}(\mathbf{Q},\omega) \\ &\quad +[1-(Q_{c^*}/|\mathbf{Q}|)^2]\,g_{c^*}^2\mathcal{S}^{x_0x_0}(\mathbf{Q},\omega) \\ &\quad +[1-(Q_{b^*}/|\mathbf{Q}|)^2]\,g_{b^*}^2\,\mathcal{S}^{y_0y_0}(\mathbf{Q},\omega)\big\}, \end{aligned} \tag{S12}$$

where $\mathbf{Q} = H\mathbf{a}^* + K\mathbf{b}^* + L\mathbf{c}^*$, $|f(Q)|^2$ is the squared form factor of Cu^{2+}, (g_a, g_{b^*}, g_{c^*}) are the relevant projections of the gyromagnetic tensor and r_0^2 sets the units of measurement. Finally, to express the components of the DSSF in conventional reciprocal-space units, we account for the centred nature of the b^*c^* plane in $CuF_2(D_2O)_2$(pyz) by defining the unit vectors of the reciprocal square lattice in terms of the crystalline reciprocal lattice as $\mathbf{e}_x = \frac{1}{2}(\mathbf{b}^* + \mathbf{c}^*)$ and $\mathbf{e}_y = \frac{1}{2}(\mathbf{b}^* - \mathbf{c}^*)$, leading to $k_x = \pi(K + L)$, $k_y = \pi(K - L)$ and $k_z = \pi H$, all of which repeat mod 2π.

B. Magnon-magnon interactions

We begin our calculations of the magnon dispersion and DSSF with a general introduction to the treatment of magnon-magnon interactions within SWT. Quite generally, interactions between magnons act to alter the quasiparticle dispersion and linewidth, causing energy renormalization, spontaneous decay and thermal decay, which lead to shifted and broadened lineshapes in the DSSF, as well as to changes in thermomagnetic quantities. These effects modify the structure and intensity of the multi-magnon continuum, including the van Hove singularities,

and can in principle create quasiparticle bound states below or even inside the multimagnon continuum.

In the SLHAF, magnon interactions originate from the expansion of Eq. (S6) in terms of Holstein-Primakoff bosons.[S6] At zero field,[S7,S8] the first non-trivial corrections originate from quartic and sextic terms in the expansion, defined in Ref.[S3] as $\hat{\mathcal{H}}_4$ and $\hat{\mathcal{H}}_6$. These terms yield corrections of order $1/S^2$ (and higher) compared to linear SWT (harmonic order, $\mathcal{O}(1)$), as we summarize in Table S1. The impact of these interactions on the zero-field one-magnon dispersion has been studied perturbatively up to order $1/S^3$,[S9] which revealed an upward renormalization of magnon energies by approximately 18% and a weak (3%) modulation of the dispersion along the Brillouin-zone boundary (associated with the slow convergence of the $1/S$ expansion around $\mathbf{k} = (\pi, 0)$). The zero-field two-magnon continuum, which carries sizable spectral weight due to the 40% zero-point moment reduction, has been computed perturbatively to order $1/S^2$.[S10] Beyond this, high-order numerical calculations for the multimagnon continuum,[S11,S12] which are made challenging by the gapless nature of the system, have been shown to account for the anomalous transverse and longitudinal multimagnon lineshapes observed in INS experiments at $\mathbf{k} = (\pi, 0)$,[S13] suggesting significant attractive magnon-magnon interactions.

When an applied magnetic field causes spin canting,[S3–S5,S14] the magnon-magnon interactions are dominated by cubic and quartic terms ($\hat{\mathcal{H}}_3$ and $\hat{\mathcal{H}}_4$). Nontrivial corrections to the magnon dispersion in finite field then emerge already at order $1/S$ (Table S1). To serve as a benchmark of our INS and MPS results, here we provide a perturbative calculation of the DSSF in this (low-field) regime, and hence include only interaction terms arising from $\hat{\mathcal{H}}_3$ and $\hat{\mathcal{H}}_4$.

C. Calculation of the magnon dispersion

The harmonic magnon dispersion of the quasi-2D SLHAF is given by diagonalizing the quadratic Hamiltonian, $\hat{\mathcal{H}}_2|\mathbf{k}\rangle = \varepsilon_{\mathbf{k}}|\mathbf{k}\rangle$, which proceeds through the Bogoliubov coefficients $u_{\mathbf{k}}$ and $v_{\mathbf{k}}$. In our notation

$$\varepsilon_{\mathbf{k}} = 2JS(2+\alpha)\sqrt{(1+\bar{\gamma}_{\mathbf{k}})(1-\cos 2\theta\,\bar{\gamma}_{\mathbf{k}})}, \quad \text{(S13)}$$

$$\bar{\gamma}_{\mathbf{k}} = (\cos k_x + \cos k_y + \alpha \cos k_z)/(2+\alpha), \quad \text{(S14)}$$

	1st Order (HF)	2nd Order (SE)
Order $1/S^2$ $(B=0)$	$\langle\hat{\mathcal{H}}_4\rangle$ and $\langle\hat{\mathcal{H}}_6\rangle$	$\hat{\mathcal{H}}_4$
Order $1/S^3$ $(B=0)$	$\langle\hat{\mathcal{H}}_4\rangle$, $\langle\hat{\mathcal{H}}_6\rangle$, $\langle\hat{\mathcal{H}}_4\hat{\mathcal{H}}_6\rangle$	$\hat{\mathcal{H}}_4$ and $\hat{\mathcal{H}}_6$
Order $1/S$ $(B\neq 0)$	$\langle\hat{\mathcal{H}}_3\rangle$ and $\langle\hat{\mathcal{H}}_4\rangle$	$\hat{\mathcal{H}}_3$

Table S1: Interaction terms retained in the perturbative treatment of the one-magnon dispersion of the SLHAF, without and with an applied magnetic field. Hartree-Fock (HF) and Self-Energy (SE) indicate the types of correction.

where $\mathbf{k} = (k_x, k_y, k_z)$ spans the cubic Brillouin zone and the classical canting angle is given by $\sin\theta = B/B_{\text{sat}} = g\mu_{\text{B}}\mu_0 B/4JS(2+\alpha)$.

For all $B \leq B_{\text{sat}}$, $1/S$ corrections to the harmonic dispersion include four terms, which we collect as the self-energy

$$\Sigma_{B\neq 0}(\mathbf{k},\omega) = \delta\varepsilon^{\text{HF}}_{\mathbf{k}} + \delta\varepsilon^{\theta}_{\mathbf{k}} + \Sigma_{31}(\mathbf{k},\omega) + \Sigma_{32}(\mathbf{k},\omega). \quad \text{(S15)}$$

The first two terms are frequency-independent, corresponding to the Hartree-Fock (mean-field) correction from $\hat{\mathcal{H}}_4$ and the canting-angle renormalization $\theta \to \bar{\theta}$ arising from $\hat{\mathcal{H}}_3$, while the other two terms are frequency-dependent and correspond to one-loop (one-bubble) magnon decay and source processes. As noted in the previous subsection, these can be contrasted with the corrections in zero field, which start at order $1/S^2$ and take the form $\Sigma_{B=0}(\mathbf{k},\omega) = \delta\varepsilon^{\text{HF}}_{\mathbf{k}} + \Sigma_{41}(\mathbf{k},\omega) + \Sigma_{42}(\mathbf{k},\omega)$, the first term being the Hartree-Fock correction from $\hat{\mathcal{H}}_4$ and $\hat{\mathcal{H}}_6$ and the other two being self-energy corrections from one-loop (two-bubble) magnon decay and source terms in $\hat{\mathcal{H}}_4$ (Table S1).[S6]

Next we compare two different approaches that have been adopted to calculate the magnon dispersion from the generic self-energy of Eq. (S15). The first calculates the corrected dispersion directly "on-shell" by inserting the harmonic magnon dispersion into the one-loop diagrams, giving

$$\bar{\varepsilon}_{\mathbf{k}} = \varepsilon_{\mathbf{k}} + \delta\varepsilon^{\text{HF}}_{\mathbf{k}} + \delta\varepsilon^{\theta}_{\mathbf{k}} + \Sigma_{31}(\mathbf{k},\varepsilon_{\mathbf{k}}) + \Sigma_{32}(\mathbf{k},\varepsilon_{\mathbf{k}}). \quad \text{(S16)}$$

The second calculates the corrected dispersion self-consistently "off-shell" as a solution of the Dyson equation, which yields

$$\varepsilon^{*}_{\mathbf{k}} = \varepsilon_{\mathbf{k}} + \delta\varepsilon^{\text{HF}}_{\mathbf{k}} + \delta\varepsilon^{\theta}_{\mathbf{k}} + \Sigma_{31}(\mathbf{k},\varepsilon^{*}_{\mathbf{k}}) + \Sigma_{32}(\mathbf{k},\varepsilon^{*}_{\mathbf{k}}). \quad \text{(S17)}$$

Both $\bar{\varepsilon}_{\mathbf{k}}$ and $\varepsilon^{*}_{\mathbf{k}}$ can acquire an imaginary part due to spontaneous decays, which adds a layer of complexity in solving the Dyson equation.[S15] In the present case, however, these decay processes are not allowed, which simplifies the calculation.

Strictly speaking, the on-shell approach is restricted to order $1/S$;[S4] however, at high fields ($B \gtrsim 0.76 B_{\text{sat}}$) it overestimates the decay of the one-magnon branch due to van Hove singularities in the two-magnon continuum once the former enters the latter. The off-shell approach regularizes this deficiency, at the expense of being more costly to calculate and breaking the consistency of the perturbative expansion, in that only some of the terms at orders higher than $1/S$ are included, which can violate the Goldstone theorem. However, at low fields the two dispersion relations $\bar{\varepsilon}_{\mathbf{k}}$ and $\varepsilon^{*}_{\mathbf{k}}$ are almost indistinguishable;[S4] because the maximum field in our experiments was only $B/B_{\text{sat}} \simeq 0.4$, well below the field-induced decay threshold, for our present analysis we compute the renormalized one-magnon dispersion on-shell ($\bar{\varepsilon}_{\mathbf{k}}$), and this is the meaning of our terminology $\overline{1/S}$-SWT.

D. Calculation of the DSSF

To obtain the DSSF corresponding to the renormalized single magnons, we first calculate its components in the local frame[S3] by introducing the one-magnon Green functions

$$G^0(\mathbf{k},\omega) = \frac{1}{\omega-\varepsilon_{\mathbf{k}}+i\delta}, \tag{S18}$$

$$\bar{G}(\mathbf{k},\omega) = \frac{1}{\omega-\bar{\varepsilon}_{\mathbf{k}}+i\delta}, \tag{S19}$$

$$G^*(\mathbf{k},\omega) = \frac{1}{\omega-\varepsilon^*_{\mathbf{k}}+i\delta}, \tag{S20}$$

$$G(\mathbf{k},\omega) = \frac{1}{\omega-\varepsilon_{\mathbf{k}}-\Sigma(\mathbf{k},\omega)}, \tag{S21}$$

where δ indicates a small positive number. Here G^0 corresponds to the case of harmonic magnons, $\bar{G}$ and G^* are the single-pole response functions calculated at the on-shell (S16) and off-shell magnon energies (S17) and G contains the full frequency-dependence of the magnon propagator in Eq. (S15), for which we use the terminology "one-magnon sidebands" (below). As discussed above, the small canting angle at low fields should make $\bar{G}$ (S19) the appropriate choice for analyzing our INS data, but we will show below that G (S21) is required to capture some of the properties of the LSM.

Within the $\overline{1/S}$-SWT framework, we calculate the one-magnon spectral function as

$$\bar{A}(\mathbf{k},\omega) = -\frac{1}{\pi}\mathrm{Im}\bar{G}(\mathbf{k},\omega), \tag{S22}$$

which yields the transverse components of the DSSF in the local frame as

$$\begin{aligned}\bar{\mathcal{S}}^{xx}(\mathbf{k},\omega) &= \pi S\Lambda_+^2(u_{\mathbf{k}}+v_{\mathbf{k}})^2\bar{A}(\mathbf{k},\omega),\\ \bar{\mathcal{S}}^{yy}(\mathbf{k},\omega) &= \pi S\Lambda_-^2(u_{\mathbf{k}}-v_{\mathbf{k}})^2\bar{A}(\mathbf{k},\omega),\end{aligned} \tag{S23}$$

where $\Lambda_\pm$ are intensity coefficients calculated for each applied field (B) and interplane coupling (α) from the numerical value of the Hartree-Fock averages.[S3] Technically, these moment-reduction factors, by which transverse spectral weight is transferred to the longitudinal channel by quantum fluctuations, also extend beyond order $1/S$, but are straightforward to include. In addition to the $\Lambda_\pm$ factors, the coefficients $u_{\mathbf{k}}$ and $v_{\mathbf{k}}$ are also calculated from the harmonic magnon dispersion to maintain the sum-rule on the trace of the DSSF. For simplicity, we proceed to the laboratory frame [Eq. (S11)] using the unrenormalized canting angle θ (rather than $\bar{\theta}$, which is almost identical at low fields).

Turning to the longitudinal component of the DSSF, in the local frame this is dominated by two-magnon excitations, which interact in principle through a one-loop process in $\hat{\mathcal{H}}_4$. However this process is of order $1/S^2$, and hence lies beyond our calculation for the one-magnon dispersion. At order $1/S$, the longitudinal DSSF is given rigorously by the density of states of two non-interacting magnons,

$$\begin{aligned}\mathcal{S}_0^{zz}(\mathbf{k},\omega) = &\frac{1}{2N}\sum_{\mathbf{p}\in\mathrm{BZ}}(u_{\mathbf{p}}v_{\mathbf{p}-\mathbf{k}}+v_{\mathbf{p}}u_{\mathbf{p}-\mathbf{k}})^2\times\\ &\mathrm{Im}\int\frac{\mathrm{d}\omega'}{2\pi i}G^0(\mathbf{p},\omega')G^0(\mathbf{k}-\mathbf{p},\omega-\omega')\\ =&\frac{1}{2N}\sum_{\mathbf{p}\in\mathrm{BZ}}(u_{\mathbf{p}}v_{\mathbf{p}-\mathbf{k}}+v_{\mathbf{p}}u_{\mathbf{p}-\mathbf{k}})^2\delta(\omega-\varepsilon_{\mathbf{p}}-\varepsilon_{\mathbf{k}-\mathbf{p}}).\end{aligned} \tag{S24}$$

Although formally correct, this expression has the disadvantage that the transverse and longitudinal response functions are calculated with magnon dispersions of different accuracies, which can become important when comparing their features as functions of energy. This deficiency is straightforward to correct, by calculating the two-magnon density of states in the longitudinal component using the renormalized one-magnon dispersions, which at the on-shell level yields

$$\bar{\mathcal{S}}^{zz}(\mathbf{k},\omega) = \frac{1}{2N}\sum_{\mathbf{p}\in\mathrm{BZ}}(u_{\mathbf{p}}v_{\mathbf{p}-\mathbf{k}}+v_{\mathbf{p}}u_{\mathbf{p}-\mathbf{k}})^2\delta(\omega-\bar{\varepsilon}_{\mathbf{p}}-\bar{\varepsilon}_{\mathbf{k}-\mathbf{p}}). \tag{S25}$$

Taken together, an appropriate SWT treatment of our $CuF_2(D_2O)_2(pyz)$ measurements combines the geometrical considerations of Eqs. (S11) and (S12) with consistent calculations of the transverse and longitudinal DSSFs [Eqs. (S23) and (S25)] that both use the on-shell magnon dispersion ($\bar{\varepsilon}_{\mathbf{k}}$) at order $1/S$ [Eq. (S16)]. Because this approach goes beyond order $1/S$ only formally, but not in execution, we refer to it as a "calculation at order $\overline{1/S}$." As already noted, we will find that the inclusion of one-magnon sidebands in $\mathcal{S}^{xx}$ and $\mathcal{S}^{yy}$ captures some of the features of our MPS calculations, and we refer to this as a "calculation at order $\overline{1/S}$ with one-magnon sidebands."

In SWT, continuous high-energy contributions (sidebands) within the transverse channels reflect the off-shell transfer of spectral weight from the one-magnon pole to the two-magnon continuum by cubic vertices. This effect can be captured by replacing $\bar{A}(\mathbf{k},\omega)$ with $A(\mathbf{k},\omega) = -1/\pi\,\mathrm{Im}\,G(\mathbf{k},\omega)$ in Eq. (S23) so that the transverse components of the DSSF in the local frame become

$$\begin{aligned}\bar{\mathcal{S}}^{xx}_{\mathrm{sb}}(\mathbf{k},\omega) &= -S\Lambda_+(u_{\mathbf{k}}+v_{\mathbf{k}})^2\mathrm{Im}\left[\frac{1}{\omega-\varepsilon_{\mathbf{k}}-\Sigma(\mathbf{k},\omega)}\right],\\ \bar{\mathcal{S}}^{yy}_{\mathrm{sb}}(\mathbf{k},\omega) &= -S\Lambda_-(u_{\mathbf{k}}-v_{\mathbf{k}})^2\mathrm{Im}\left[\frac{1}{\omega-\varepsilon_{\mathbf{k}}-\Sigma(\mathbf{k},\omega)}\right].\end{aligned} \tag{S26}$$

This transfer also affects the longitudinal component, which we describe by introducing a quasiparticle-residue formulation for the one-magnon Green function,[S15]

$$G(\mathbf{k},\omega) \approx \frac{Z_{\mathbf{k}}}{\omega-\bar{\varepsilon}_{\mathbf{k}}+i\delta}+G_{\mathrm{inc}}(\mathbf{k},\omega) \tag{S27}$$

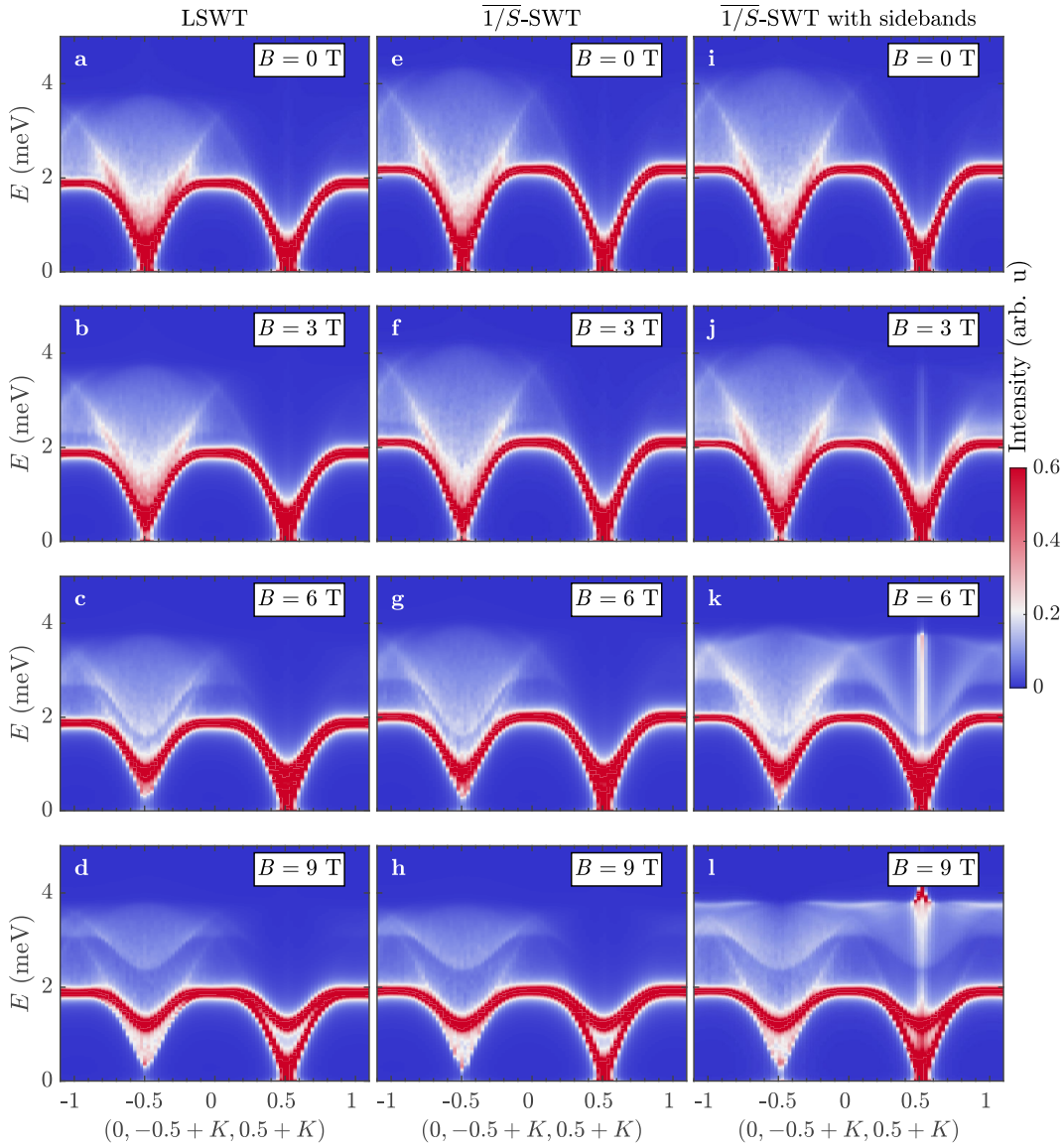

Figure S12: **DSSF along MXM from $\overline{1/S}$-SWT.** DSSFs corresponding to momentum transfer $(0, -0.5+K, 0.5+K)$ in the LET experiment, shown for all four applied magnetic fields. **a-d** Linear SWT including two-magnon states calculated using the harmonic magnon dispersion. **e-h** $\overline{1/S}$-SWT, with both one- and two-magnon excitations calculated on-shell. **i-l** $\overline{1/S}$-SWT with additional sidebands allowed for the one-magnon excitations; the vertical line of intensity around $(0, 0, 1)$ is an artifact of the off-shell calculation that is also present, but masked, in Ref.[S3]

with

$$Z_{\mathbf{k}} = \mathrm{Re}\left[1 - \frac{\partial \Sigma(\mathbf{k}, \omega)}{\partial \omega}\right]^{-1}_{\omega=\bar{\varepsilon}_{\mathbf{k}}}. \tag{S28}$$

The advantage of this formulation is that the quasiparticle pole can be inserted directly into the longitudinal DSSF,

$$\bar{\mathcal{S}}^{zz}_{\mathrm{sb}}(\mathbf{k}, \omega) = \frac{1}{2N} \sum_{\mathbf{p} \in \mathrm{BZ}} Z_{\mathbf{p}} Z_{\mathbf{k}-\mathbf{p}} (u_{\mathbf{p}} v_{\mathbf{k}-\mathbf{p}} + v_{\mathbf{p}} u_{\mathbf{k}-\mathbf{p}})^2 \times \delta(\omega - \bar{\varepsilon}_{\mathbf{p}} - \bar{\varepsilon}_{\mathbf{k}-\mathbf{p}}), \tag{S29}$$

at the expense of neglecting the incoherent sidebands ($G_{\mathrm{inc}}(\mathbf{k}, \omega)$ in Eq. (S27)).

E. Calculation and results

We computed the DSSF within $\overline{1/S}$-SWT by using and improving the Matlab code developed in Ref.[S3] for the quasi-2D SLHAF. In all of these calculations, Hartree-Fock averages for a given B and α were computed using Simpson's Rule on a 1000^3 grid to obtain six-digit accuracy. Unless otherwise noted, all self-energy calcu-

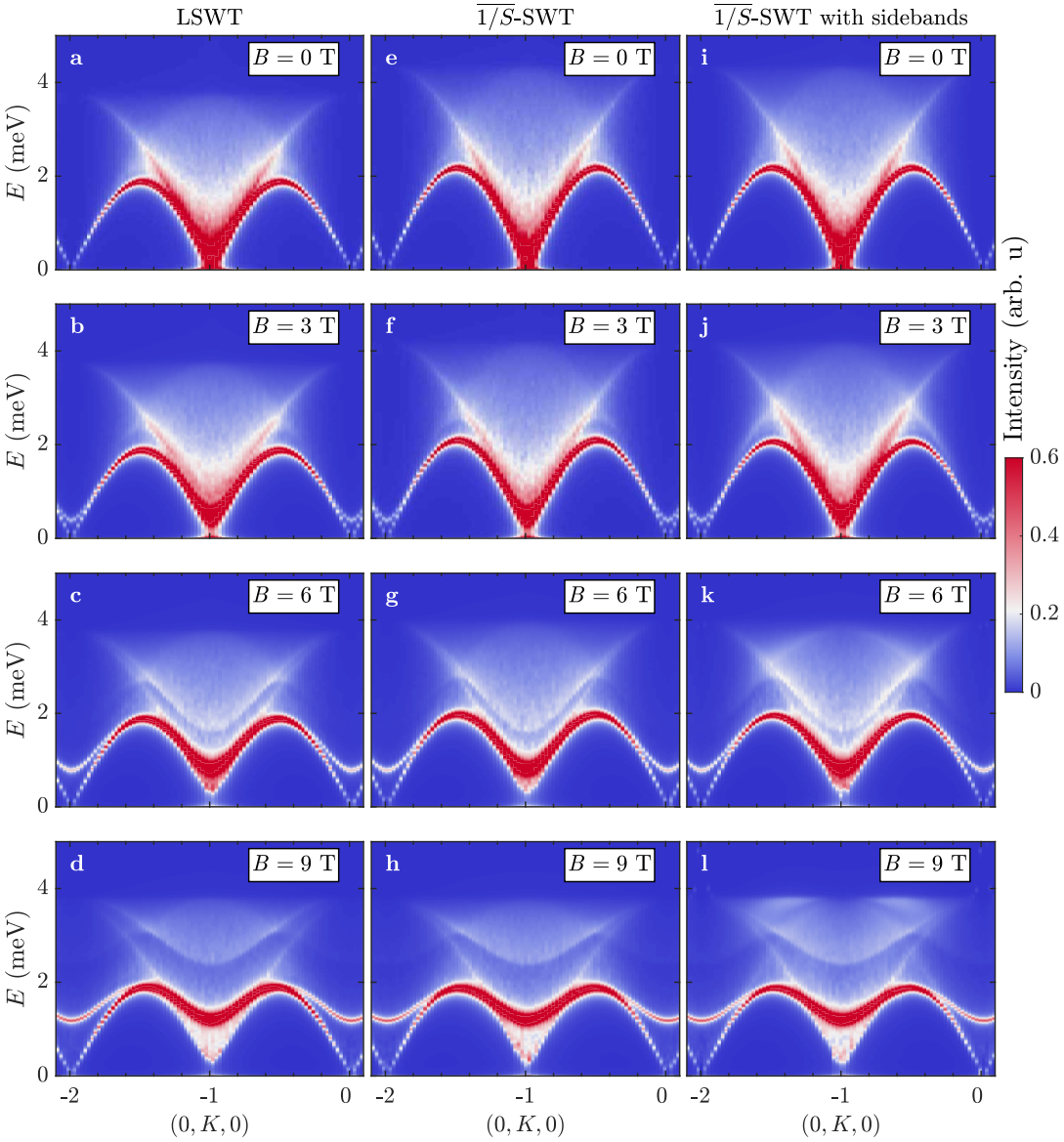

Figure S13: **DSSF along ΓMΓ from $\overline{1/S}$-SWT.** As in Fig. S12 for momentum transfer $(0, K, 0)$.

lations were performed using the Monte Carlo method with $N_{\mathrm{MC}} \geq 10^5$ and Brillouin-zone integrals for the two-magnon density of states with $N_{2\mathrm{M}} \geq 10^4$. In the following we use a small Lorentzian broadening of $\delta = 0.05$ meV in our colour contour figures, $\delta = 0.03$ meV for line cuts that compare $\overline{1/S}$-SWT with MPS and INS and $\delta = 0.005$ meV to study the positions of van Hove singularities.

The results of these calculations at the different levels of approximation are presented in Figs. S12 and S13 for the momentum-energy scans shown in Fig. 2 of the main text. Other than the artifact of the off-shell calculation appearing around the centre of the magnetic Brillouin zone, the $\overline{1/S}$ calculation with sidebands captures more features of the INS and MPS data, and thus we adopt this level of approximation in the discussion to follow. SWT is particularly valuable for interpreting the DSSFs of the different spin channels, and hence in Figs. S14 and S15 we present the channel-resolved response functions for a field corresponding to $B = 9$ T, with the polarization factor and canting-angle corrections applied. These calculations correspond to the MPS results shown in Figs. S8 and Fig. S9.

F. Two-magnon resonance in the continuum

It is clear from Figs. S12-S15 that SWT at this level does not capture the LSM we observe by INS and MPS. As in Figs. 4d and 4h of the main text, the two-magnon continuum within $\overline{1/S}$-SWT remains broadly distributed in energy at all wavevectors. This reflects the fact that

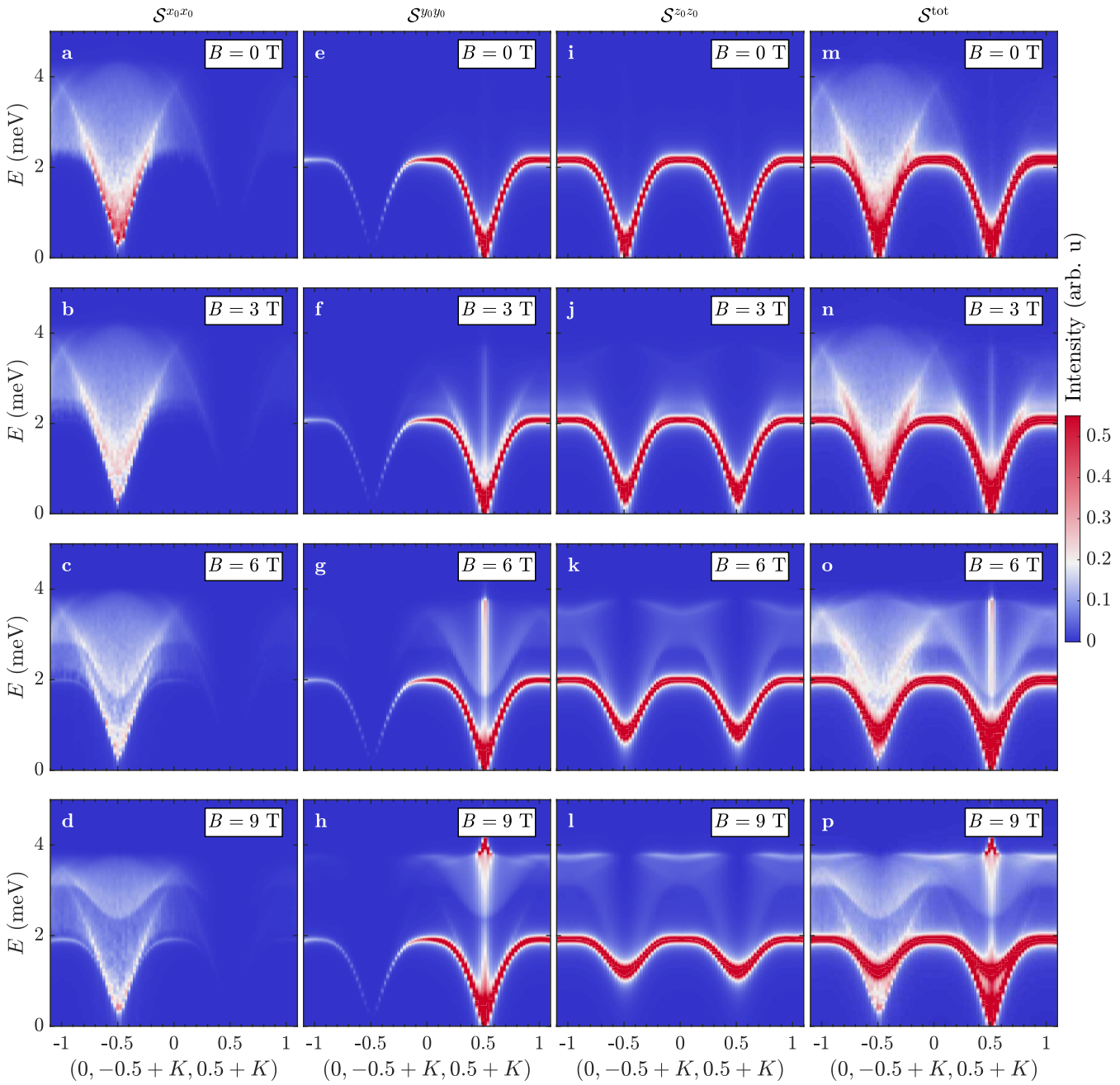

Figure S14: **Channel-resolved DSSF along MXM from $\overline{1/S}$-SWT.** DSSF components $\mathcal{S}^{x_0x_0}$ (a-d), $\mathcal{S}^{y_0y_0}$ (e-h), $\mathcal{S}^{z_0z_0}$ (i-l) and their sum, denoted $\mathcal{S}_{\mathrm{tot}}$ (m-p), shown at the four magnetic fields of the LET experiment for momentum transfer $(0, -0.5 + K, 0.5 + K)$, calculated by $\overline{1/S}$-SWT with additional sidebands allowed for the one-magnon excitations.

$\overline{1/S}$-SWT includes magnon interaction effects only at the level of a self-energy of individual magnons, and does not contain direct magnon-magnon interactions in the calculation of the continuum. In this way our $\overline{1/S}$-SWT calculation allows us to benchmark the type of physical processes that give rise to a resonance as sharp as the LSM. As noted above, the effects of these magnon-magnon interactions have been captured by a numerical high-order expansion,[S11,S12] although to date this has been performed only at zero field and not in a state with canted magnetic order.

However, our $\overline{1/S}$–SWT calculations show that including sidebands (Figs. S12i-l and S13i–l) does produce a continuum edge across the full momentum range, which matches the location of the LSM. Without sideband effects, the continuum arises only from the longitudinal x_0x_0 and z_0z_0 channels, and is therefore suppressed very strongly at $(0, 0, 1)$ and $(-2, 0, 0)$ by polarization factors and the small canting angle, leaving it visible only near $(0, 1, 0)$ (Figs. S12e-h and S13e-h). Sidebands transfer

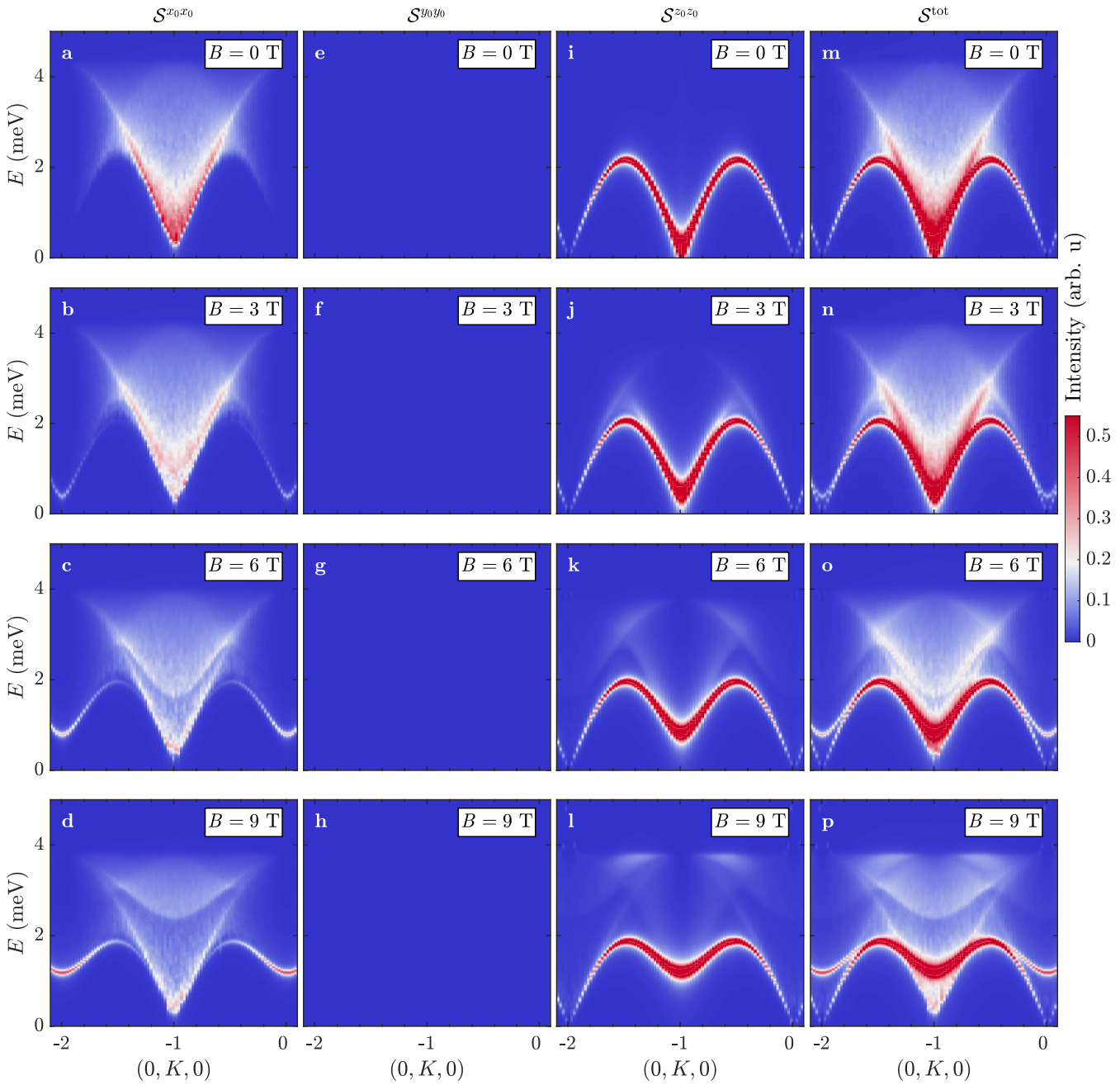

Figure S15: **Channel-resolved DSSF along ΓMΓ from $\overline{1/S}$-SWT.** As in Fig. S14 for momentum transfer $(0, K, 0)$.

spectral weight into the transverse y_0y_0 channel, which is not suppressed at $(0, 0, 1)$, thereby restoring a continuum edge across the full **Q** range. At $(-2, 0, 0)$ this transverse channel is again suppressed, as observed in experiment. Physically, sidebands redistribute weight from the one-magnon mode into the two-magnon continuum in a way that produces a more isotropic spin response than bare $\overline{1/S}$-SWT can capture.

Because this edge feature in the continuum tracks the position of the LSM, we presume that it can be considered as providing a basis for the strong bootstrapping effect of magnon-magnon interactions that results in the

p	**q**	$f(\mathbf{p}, \mathbf{q})$	Singularity Type
L	ZB	$\varepsilon_{\mathrm{ZB}} + \Delta + \alpha(\tilde{p}_x^2 + \tilde{p}_y^2) - \beta_x \tilde{q}_x^2 - \beta_y \tilde{q}_y^2$	Logarithmic
L	G	$\Delta + \alpha(\tilde{p}_x^2 + \tilde{p}_y^2) + c\lvert\tilde{\mathbf{q}}\rvert$	Power-law
L	L	$2\Delta + \alpha(\tilde{p}_x^2 + \tilde{q}_x^2 + \tilde{p}_y^2 + \tilde{q}_y^2)$	Step

Table S2: Nature of van Hove singularities involving the Larmor mode in the two-magnon density of states, $\mathcal{D}_2(\mathbf{k}, \omega)$, in the low-field regime as a function of the independent momenta **p** and **q** contributing to the density of states. L denotes Larmor, ZB zone-boundary and G Goldstone.

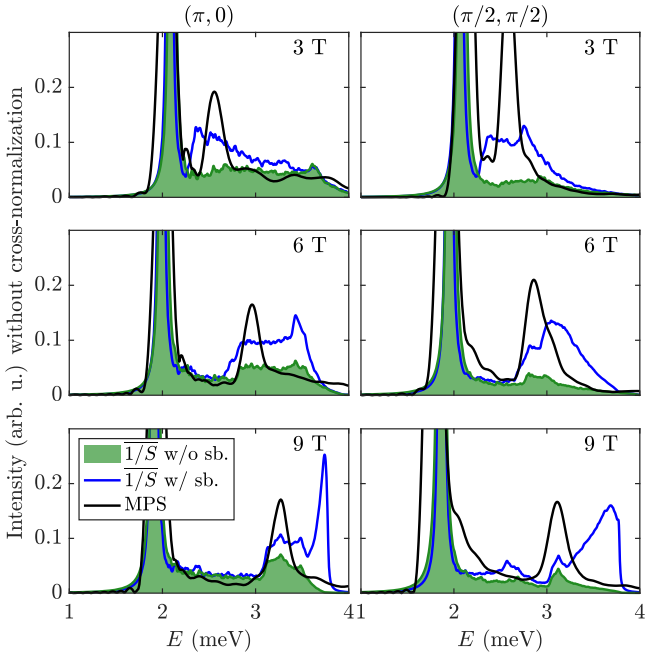

Figure S16: **Van Hove singularities in the two-magnon density of states.** Comparison between the positions of van Hove singularities in the SWT continuum and the LSM predicted by MPS.

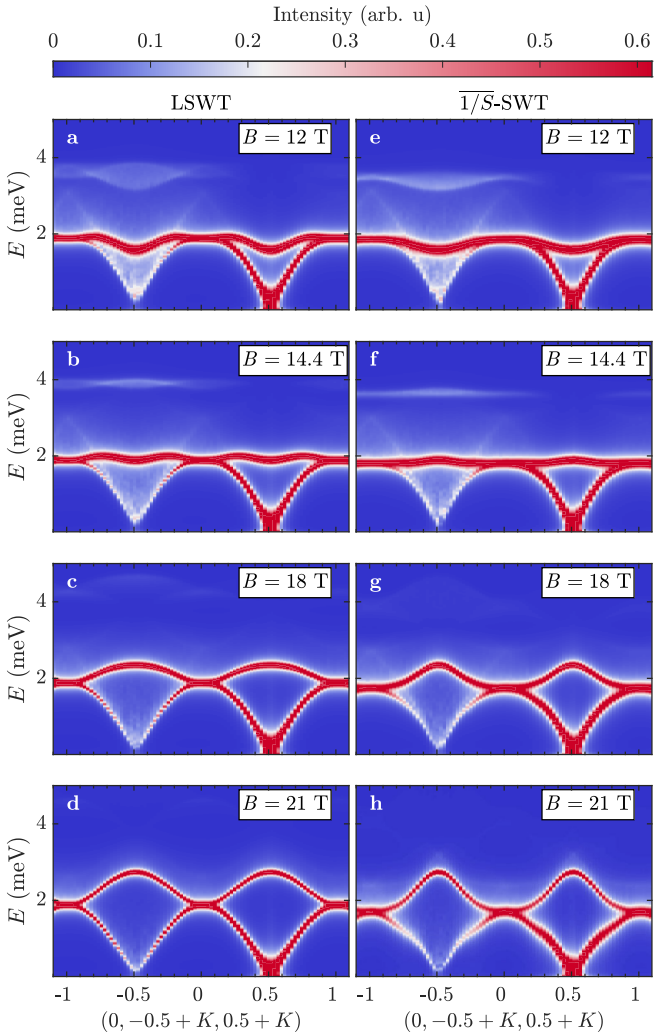

Figure S17: **High-field DSSF along MXM from $\overline{1/S}$-SWT.** DSSFs corresponding to momentum transfer $(0, -0.5 + K, 0.5 + K)$ for fields in the vicinity of half saturation, which are beyond the range of our experiment. **a-d** Linear SWT including two-magnon states calculated using the harmonic magnon dispersion. **e-h** $\overline{1/S}$-SWT with both one- and two-magnon excitations calculated on-shell.

appearance of a sharp resonance within the continuum. To trace the origin of this feature, we consider the presence and nature of van Hove singularities in the two-magnon density of states of the SLHAF. We proceed for simplicity by using harmonic magnons, but this aspect of the analysis is the same for the renormalized dispersions $\bar{\varepsilon}_{\mathbf{k}}$ and $\varepsilon^*_{\mathbf{k}}$. At the low magnetic fields we consider, the DSSF is dominated by three regions of the Brillouin zone where the dispersion is either nearly massless or disperses quadratically away from a flat region around an extremum. Denoting small wavevectors away from the extrema by $\tilde{\mathbf{k}}$, these are: (i) the Larmor mode near $\mathbf{k} = 0$ which is a local minimum ($\alpha > 0$)

$$\varepsilon^{\mathrm{L}}_{\mathbf{k}} \approx \Delta + \alpha(\tilde{k}_x^2 + \tilde{k}_y^2), \tag{S30}$$

where $\Delta = g\mu_B B$ is unaffected by quantum corrections due to the Larmor theorem; (ii) the zone-boundary excitations extending from $\mathbf{k} = (\pi, 0)$ to $(\pi/2, \pi/2)$,

$$\varepsilon^{\mathrm{ZB}}_{\mathbf{k}} \approx \varepsilon_{\mathrm{ZB}} - \beta_x \tilde{k}_x^2 - \beta_y \tilde{k}_y^2, \text{ with } \varepsilon_{\mathrm{ZB}} = 4JS, \tag{S31}$$

which present a global maximum ($\beta_{x,y} > 0$ at low fields); (iii) the Goldstone mode near $\mathbf{k} = (\pi, \pi)$,

$$\varepsilon^{\mathrm{G}}_{\mathbf{k}} \approx c|\tilde{\mathbf{k}}|, \text{ with } c = 2\sqrt{2}JS, \tag{S32}$$

which is a global minimum.

The two magnon density of states,

$$\mathcal{D}_2(\mathbf{k}, \omega) = \frac{1}{N} \sum_{\mathbf{p} \in \mathrm{BZ}} \delta(\omega - \varepsilon_{\mathbf{p}} - \varepsilon_{\mathbf{q}=\mathbf{k}-\mathbf{p}}), \tag{S33}$$

displays van Hove singularities when the function $f(\mathbf{p}, \mathbf{q}) = \varepsilon_{\mathbf{p}} + \varepsilon_{\mathbf{q}=\mathbf{k}-\mathbf{p}}$ has extrema. In general, local minima and maxima give rise to step singularities, while saddle points produce logarithmic divergences, which are more pronounced. In Table S2 we follow Ref.[S5] to classify the three types of singularity involving the Larmor mode, in order of decreasing strength, as functions of the independent momenta $\mathbf{p}$ and $\mathbf{q} \equiv \mathbf{k} - \mathbf{p}$. All of these singularities contribute at least a step discontinuity to the continuum edge that tracks the position of the LSM, with the strongest singularity (logarithmic) originating from the combination of a Larmor mode with zone-boundary magnons. In this way even linear SWT provides additional insight into the physics underlying the emergence of a non-perturbative resonance in the

continuum as strong as the Larmor-shadow mode. In Fig. S16, we compare the spectral functions calculated by $1/S$–SWT with sidebands to our MPS results for the two zone-boundary wavevectors of Fig. 5 at 3, 6 and 9 T, which enables us to relate the positions of the van Hove singularities in SWT with the actual position of the LSM.

Finally, in Fig. S17 we use our $1/S$-SWT framework to compute the spectral function at applied magnetic fields around and above half saturation ($B_{\rm sat}/2 = 14.4$ T). At this field the Larmor mode in linear SWT transforms in from a local minimum to a global maximum of the magnon dispersion, and this change is clearly associated with the disappearance of any enhanced density-of-states effects in the two-magnon continuum. As noted in the main text, we expect on this basis that the LSM ceases to exist for fields above half saturation, which would be consistent with the collapse of the shadow feature observed in the honeycomb-lattice Heisenberg antiferromagnet.[S16]

[S1] Lanza, A. *et al.* New magnetic frameworks of $[(CuF_2(H_2O)_2)_x(pyz)]$. *Chem. Commun.* **50**, 14504–14507 (2014).

[S2] Lüscher, A. & Läuchli, A. M. Exact diagonalization study of the antiferromagnetic spin-$\frac{1}{2}$ Heisenberg model on the square lattice in a magnetic field. *Phys. Rev. B* **79**, 195102 (2009).

[S3] Fuhrman, W. T., Mourigal, M., Zhitomirsky, M. E. & Chernyshev, A. L. Dynamical structure factor of quasi-two-dimensional antiferromagnet in high fields. *Phys. Rev. B* **85**, 184405 (2012).

[S4] Zhitomirsky, M. E. & Chernyshev, A. L. Instability of antiferromagnetic magnons in strong fields. *Phys. Rev. Lett.* **82**, 4536–4539 (1999).

[S5] Mourigal, M., Zhitomirsky, M. E. & Chernyshev, A. L. Field-induced decay dynamics in square-lattice antiferromagnets. *Phys. Rev. B* **82**, 144402 (2010).

[S6] Zhitomirsky, M. E. & Chernyshev, A. L. Colloquium: Spontaneous magnon decays. *Rev. Mod. Phys.* **85**, 219 (2013).

[S7] Canali, C. M., Girvin, S. M. & Wallin, M. Spin-wave velocity renormalization in the two-dimensional Heisenberg antiferromagnet at zero temperature. *Phys. Rev. B* **45**, 10131–10134 (1992).

[S8] Igarashi, J.-i. $1/S$ expansion for spin-wave theory in two-dimensional Heisenberg antiferromagnets. *Phys. Rev. B* **46**, 10763–10774 (1992).

[S9] Syromyatnikov, A. V. Spectrum of short-wavelength magnons in a two-dimensional quantum Heisenberg antiferromagnet on a square lattice: third-order expansion in $1/S$. *J. Phys.: Condens. Matter* **22**, 216003 (2010).

[S10] Elliott, R. J. & Thorpe, M. F. The effects of magnon-magnon interaction on the two-magnon spectra of antiferromagnets. *J. Phys. C: Solid State Phys.* **2**, 1630–1644 (1969).

[S11] Powalski, M., Uhrig, G. S. & Schmidt, K. P. Roton Minimum as a Fingerprint of Magnon-Higgs Scattering in Ordered Quantum Antiferromagnets. *Phys. Rev. Lett.* **115**, 207202 (2015).

[S12] Powalski, M., Schmidt, K. P. & Uhrig, G. S. Mutually attracting spin waves in the square-lattice quantum antiferromagnet. *SciPost Phys.* **4**, 001 (2018).

[S13] Dalla Piazza, B. *et al.* Fractional excitations in the square-lattice quantum antiferromagnet. *Nat. Phys.* **11**, 62 (2014).

[S14] Zhitomirsky, M. E. & Nikuni, T. Magnetization curve of a square-lattice Heisenberg antiferromagnet. *Phys. Rev. B* **57**, 5013–5022 (1998).

[S15] Chernyshev, A. L. & Zhitomirsky, M. E. Spin waves in a triangular lattice antiferromagnet: Decays, spectrum renormalization, and singularities. *Phys. Rev. B* **79**, 144416 (2009).

[S16] Hernández, J. A. *et al.* Field-Induced Magnon Decay, Magnon Shadows, and Roton-like Excitations in the Honeycomb Antiferromagnet $YbBr_3$. *Phys. Rev. Lett.* **135**, 146701 (2025).